Mixed-Field Radiation Monitoring and Beam Characterization Through Silicon Diode Detectors

Kacper Biłko, *Graduate Student Member, IEEE*, Rubén García Alía, *Member, IEEE*, Mario Sacristan Barbero, *Member, IEEE*, Sylvain Girard, *Senior Member, IEEE*, Ygor Aguiar, *Member, IEEE*, Matteo Cecchetto, Camille Belanger-Champagne, *Member, IEEE*, Salvatore Danzeca, Wojtek Hajdas, Alex Hands, Pedro Martín Holgado, *Student Member, IEEE*, Yolanda Morilla Garcia, Amor Romero Maestre, Daniel Prelipcean, Federico Ravotti, *Member, IEEE*, and Marc Sebban

***Abstract*— We present a calibration of a commercial silicon diode with proton and alpha beams and gamma rays. The diode together with a fast acquisition chain can be exploited for both direct and indirect (through the secondary radiation field) beam characterization. Within this work, we demonstrate the detector capabilities of resolving single-energy-deposition events and independently measuring dose rate and beam flux. Profiting from the mixed radiation field in CERN's high-energy accelerator mixed field facility (CHARM) we show how the silicon detector can be exploited to characterize the mixed radiation field present in it, which in turn is used for validating the radiation tolerance of components and systems to be installed in the European Organization for Nuclear Research (CERN) accelerator complex.**

***Index Terms*— CERN high-energy accelerator mixed field facility (CHARM), CERN radiation monitor (RadMon), diode, FLUKA, mixed-field, silicon, simulations, total ionizing dose (TID).**

I. Introduction

IN HIGH-ENERGY and high-intensity accelerators, even a small amount of beam losses lead to a radiation field in its immediate surroundings. Depending on the beam energy, the secondary radiation field consists of multiple particle species at various energies (mixed-field radiation). In the largest European Organization for Nuclear Research (CERN) accelerators, such as large hadron collider [1], [2], [3] or super proton synchrotron (PS) [4], the induced radiation poses a threat to the reliability of the installed electronic systems. Therefore, CERN's radiation hardness assurance (RHA) approach requires: 1) knowledge about the expected radiation environment that is provided by the beam monitoring and simulations and 2) radiation-tolerant design of electronic systems. The CERN in-house designs are based often on the commercial-off-the-shelf (COTS) components, which require radiation tests, both at the component (before the system design) and system levels. In the case of CERN, the latter is performed in the CERN high-energy accelerator mixed field facility (CHARM) [5]. The radiation field, produced via the spallation reaction with a target, mimics the mixed radiation field that can be encountered along the CERN accelerator infrastructure.

In addition to system-level irradiation tests, the CHARM facility is used as a validation for dosimeters and radiation monitors intended for the accelerator's mixed-field monitoring, for example, for distributed optical fiber radiation sensor (DOFRS) [6] or CERN radiation monitors (RadMons) [7], [8]. The facility provides multiple instruments for radiation monitoring, together with the validated simulations in the FLUKA Monte Carlo code [9], [10], [11], [12].

This work extends the previous studies that demonstrated the use of a 300-μm passivated implanted planar silicon (PIPS) detector for heavy-ion beam characterization [13], [14], [15], to a characterization of the CHARM's mixed-field. When compared to a previous study [16], the measurements involve an additional radiation-exposed location ($m5$) and provide the intercomparison with the standard beam instrumentation available in the facility. This is exploited for the indirect beam characterization through the secondary mixed field, for example, for the spill duration optimization. The presented silicon detector is intended to be used as a complementary instrument for CHARM monitoring, and in the future, for the accelerator's mixed-field radiation environment [17].

Manuscript received 12 November 2023; revised 27 December 2023; accepted 2 January 2024. Date of publication 5 January 2024; date of current version 18 April 2024. This work was supported in part by the European Union's Horizon 2020 Research and Innovation Program under Grant 101008126. TRIUMF beam time was funded by the European Union's 2020 Research and Innovation Program, corresponding to the RADNEXT project. *(Corresponding author: Kacper Biłko.)*

Kacper Biłko is with the European Organization for Nuclear Research (CERN), 1211 Geneva, Switzerland, and also with Laboratoire Hubert Curien, Université Jean Monnet, 42000 Saint-Étienne, France (e-mail: kacper.bilko@cern.ch).

Rubén García Alía, Mario Sacristan Barbero, Ygor Aguiar, Matteo Cecchetto, Salvatore Danzeca, Daniel Prelipcean, and Federico Ravotti are with the European Organization for Nuclear Research (CERN), 1211 Geneva, Switzerland.

Sylvain Girard is with Laboratoire Hubert Curien, Université Jean Monnet, 42000 Saint-Étienne, France, and also with the Institut Universitaire de France (IUF), Ministère de l'Enseignement Supérieur et de la Recherche, 75 231 Paris, France.

Camille Belanger-Champagne and Alex Hands are with TRIUMF, Vancouver, BC V6T 2A3, Canada.

Wojtek Hajdas is with the Paul Scherrer Institut (PSI), 5232 Villigen, Switzerland.

Pedro Martín Holgado, Yolanda Morilla Garcia, and Amor Romero Maestre are with the Centro Nacional de Aceleradores, Universidad de Seville, Consejo Superior de Investigaciones Científicas (CSIC), Junta de Andalucía (JA), E-41092 Seville, Spain.

Marc Sebban is with Laboratoire Hubert Curien, Université Jean Monnet, 42000 Saint-Étienne, France.

Color versions of one or more figures in this article are available at https://doi.org/10.1109/TNS.2024.3350342.

Digital Object Identifier 10.1109/TNS.2024.3350342

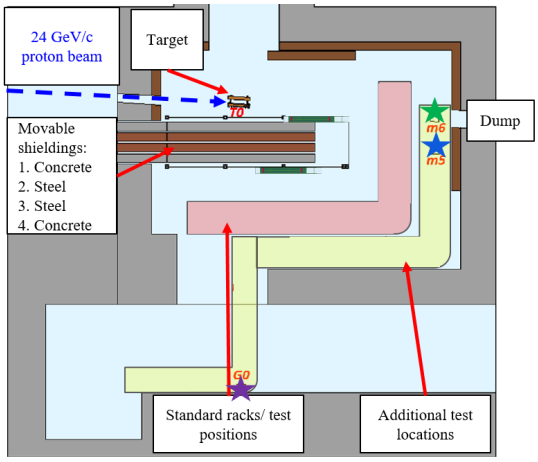

Fig. 1. Schematic top view drawing of the CHARM facility with the highlighted detector testing positions: $m5$, $m6$, and $G0$. Adapted from: [12].

The article is structured as follows: Section II introduces the CHARM facility, where mixed-field measurements were performed, and the silicon diode detectors that were used in this study. Section III presents the calibration of the detectors with proton and alpha beams performed at Centro Nacional de Aceleradores (CNA; Seville, Spain). The section shows as well dose-rate calibration with the Co-60 source provided at the same facility. Section IV describes the proton measurements from Paul Scherrer Institut (PSI) and TRIUMF facilities, which are used to demonstrate the capabilities and limitations of the detector in the case of direct beam characterization (based on the interaction of the primary beam with the silicon). Section V demonstrates the use of the detector in mixed-field radiation environments, similar to ones present near the accelerators. Section VI exploits the use of the detector for a beam characterization through the secondary mixed field. Section VII contains the summary of the work with the related outlook.

II. Experimental Setup

A. CHARM Facility

The CHARM facility [5] is part of CERN's PS East Area [18]. It provides a mixed field through a spallation reaction between 24 GeV/c protons from a PS and a target (the most frequently Cu). In addition to the target selection, the facility allows the modification of the particle spectral composition by the shielding arrangement. CHARM contains several standard test locations, varying in terms of particle spectra and intensity. Within the scope of this work, measurements at two positions were performed: $G0$ and $m5$. During tests, the copper target was used and no shielding was in place. The schematic drawing with the highlighted testing positions is depicted in Fig. 1.

B. Canberra Silicon Diode Detectors

The experimental setup, depicted in Fig. 2, is based on the Canberra FD 50-14-300RM commercial silicon detectors. Within this work, measurements from three detectors (the same model) are presented. The detectors were operated in the reverse-bias mode, under a voltage listed in Table I, that according to the manufacturer is sufficient to obtain a full depletion.

TABLE I
Specification of the Used Canberra FD 50-14-300RM Detectors

Ref.	Lot number	Applied bias (V)	Thickness (mm)	Exposed Si surface (cm^2)
I	3184.318.119.14	110	0.3	0.5
II	3705.326D.377.21	60	0.3	0.5
III	3705.326D.378.18	60	0.3	0.5

Whereas the exposed surface is equal to 0.5 cm^2, this model of detectors is known to have some silicon active volume under the steel case [13]. Based on the ratio of direct ionization events from: 1) heavy ions directly punching silicon and 2) heavy ions degraded by the case before the interaction [14], we estimate the actual sensitive region to be in the 0.75–0.85 cm^2, that is, up to 70% larger. This was reflected in the FLUKA Monte Carlo model of the detector depicted in Fig. 3.

Both detectors were operated with either of two CIVIDEC preamplifiers: C1-HV or C2-HV. The certified gain was equal to 21.7 and 43.9 dB, respectively. The amplified output signal was digitized with the CAEN DT5751 1 GS/s digitizer.

III. Detector Calibration

A. Energy Calibration at CNA

Each energy deposition event is recorded as a voltage trace over time. After the conversion ($R = 50\ \Omega$ impedance) to current, the signal is integrated to retrieve the number of the collected charges. This step assumes that the setup does not encounter signal losses and the amplification is equal to the one specified by CIVIDEC. In the following step, the total deposited energy is calculated as the measured number of charges multiplied by the energy that is needed to create an e-hole pair in silicon ($W \approx 3.6$ eV). On top of that, the obtained deposited energy value is further multiplied by a k correction factor, arising from a calibration.

For both detectors, the calibrations were performed in the 3-MV Tandem accelerator at CNA under vacuum conditions, as depicted in Fig. 4 [19], [20]. In the case of detector I, the calibration involved a proton beam with ten energies between 0.5 and 2.97 MeV, also exploitable for electronics testing [21]. Detector II was calibrated with an alpha beam of four different energies between 2.97 and 8.95 MeV. The obtained k factors are equal to 0.95 in the case of detector I and 0.92 for detector II. The factors are similar and the difference is likely due to the detectors themselves (e.g. due to the irradiation history and/or doping difference). As it has been reported [22], the value might depend on the depositing particle type. Within the accuracy of the presented setup, there is no evidence that the difference in k factors comes from the different particle types used during the calibration (proton, alpha), mainly thanks to a very thin dead layer (<50 nm).

B. Dose-Rate Calibration With Co-60 at CNA

A current that is measured at the preamplifier's bias output is directly proportional to the dose rate. Profiting from this fact, a calibration of the setup (detector II) against Co-60 was performed. During the test, the beam was not collimated and the detector was covered with an aluminum foil. The reference

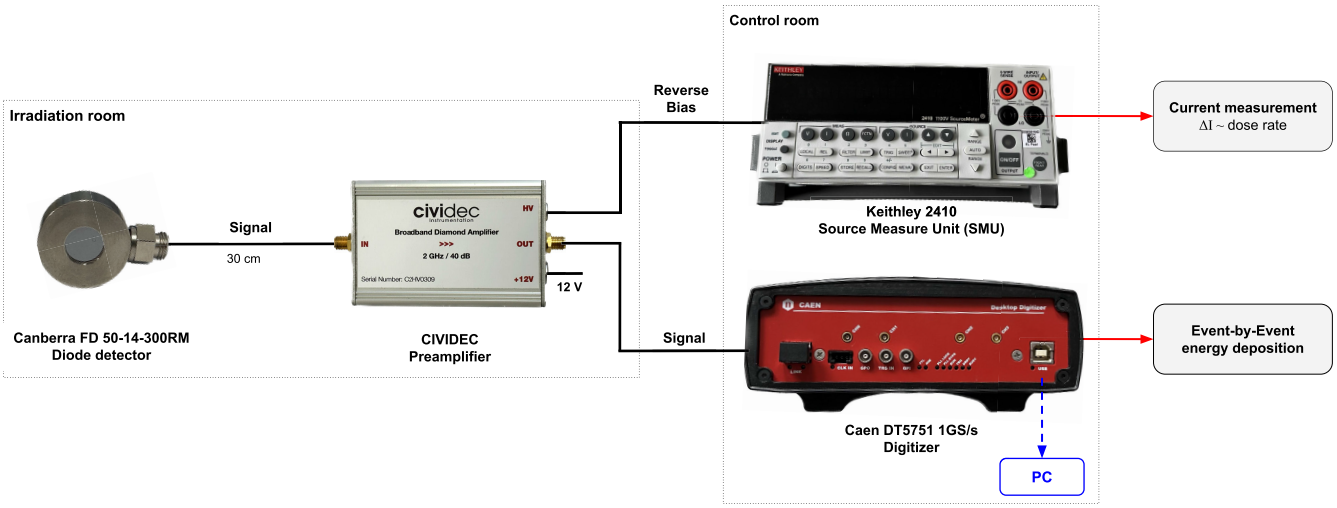

Fig. 2. Scheme of the experimental setup used in this study, consisting of a silicon diode detector, power supplies, a preamplifier, and a digitizer.

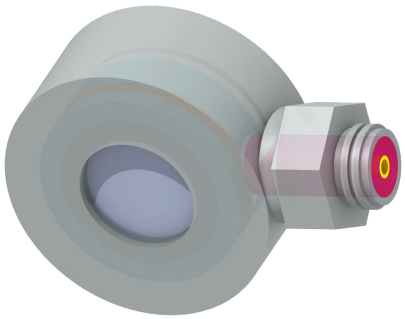

Fig. 3. Model of the detector implemented in the FLUKA Monte Carlo particle transport code.

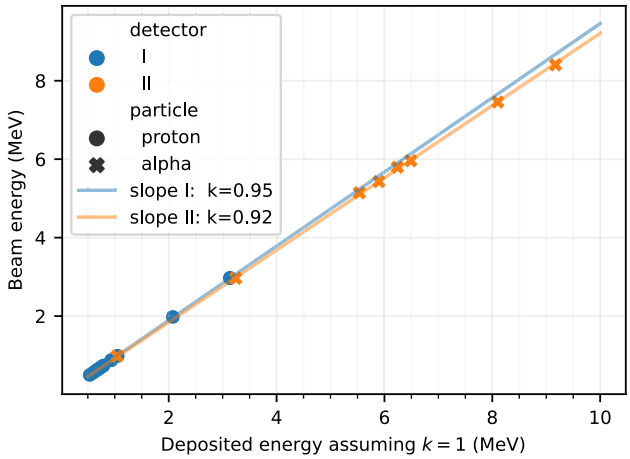

Fig. 4. Total deposited energy (equal to the beam energy) as a function of the measured deposited energy that assumes on average 3.6 eV to create a single e-hole pair and setup parameters according to the specification. The calibration was performed for both detectors (I and II) listed in Table I. The slope of each fit corresponds to a correction factor k that should be applied to the measurements in a similar energy regime.

dose-rate measurements in the facility were obtained using PTW 30010 Farmer ionization chamber (volume 0.6 cm^3, with a 4.55-mm-thick polymethyl methacrylate (PMMA) build-up cap). The measurements with the linear fit are depicted in Fig. 5. The retrieved current to dose-rate conversion is equal to 6.2×10^4 Gy/s/A.

It has to be noted that the presented detector contains a case that partially covers the active silicon region, as described in Section II-B. During the calibration with gammas from

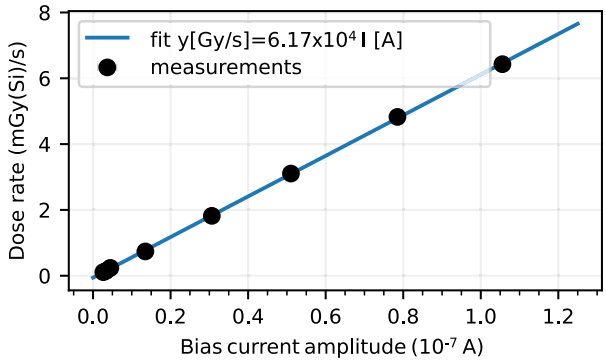

Fig. 5. Dose-rate (in Si) as a function of the leakage current amplitude under the Co-60 irradiation (detector II).

Co-60, the case helps in reaching the electron equilibrium, which would not be achieved if pure 300-μm-thick silicon was used, as there would not be enough material for electron build-up. The electron equilibrium was achieved in the reference condition, in the used ionization chamber. According to performed FLUKA Monte Carlo simulations under irradiation with photons of 1 MeV, the measured dose would be within 30% lower when compared with the dose in thicker silicon volume (in electron equilibrium). While considering only the active region itself and without surroundings, the respective dose would be factor 3.3 underestimated.

The calibration is useful for dose rate estimations in high-radiation environments, where the use of event-by-event acquisition mode is not feasible due to pile-ups. With the presented limitations due to potential case impact, the uncertainty of the dose rate measurements in a mixed-field is within 41%, as the calibration could introduce 30% overestimation due to electron-equilibrium condition and the case collimation (assuming the worst case of 0.35 cm^2 shielded surface) could reduce the active silicon volume by 41%, leading to the dose rate underestimation. However, in the accelerator's mixed field, for example, in CHARM, the expected deviation would be lower due to the highly penetrating nature of the radiation.

IV. Direct Beam Characterization

This section profits from the previously described calibration and applies it to the measurements with proton

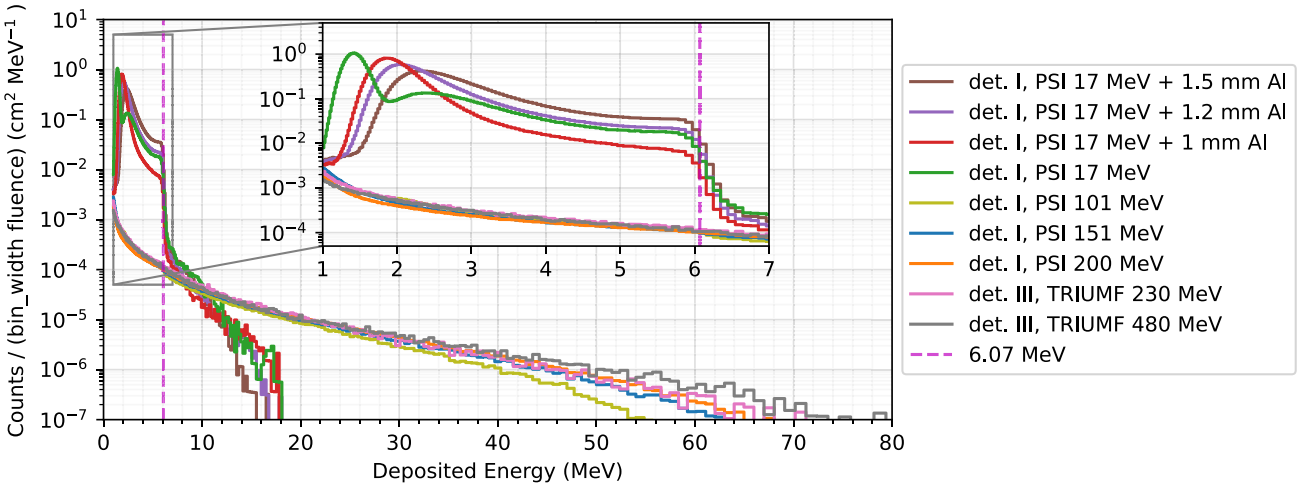

Fig. 6. Energy deposition spectra under proton irradiations as measured by detector I (PSI-PIF) and detector III (similar to detector II, TRIUMF-PIF). Additionally, at 6.07 MeV, a vertical dashed line is displayed, which indicates the maximum energy that a proton can deposit in 300 μm of silicon through electromagnetic interactions.

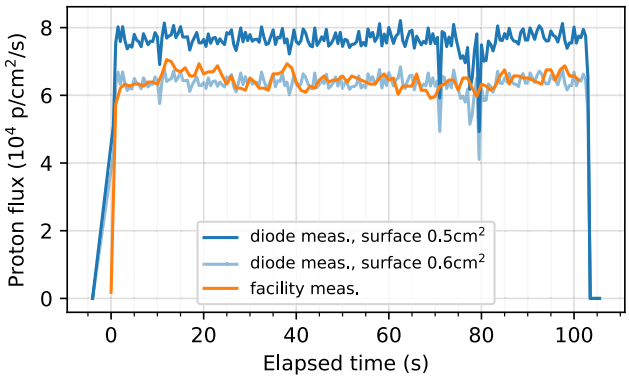

Fig. 7. Flux over time as measured by detector I, via the event-by-event energy depositions, in PSI-PIF facility for 17-MeV protons, together with the flux profile provided by the facility. The calculation for the diode assumes that the exposed Si surface (0.5 cm^2) is the only active surface. However, some protons punchthrough the diode case.

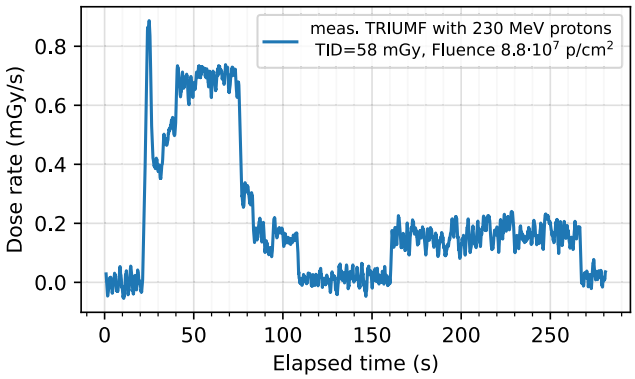

Fig. 8. Dose-rate (in Si) during the irradiation with 230-MeV protons in TRIUMF-PIF, as measured by detector III, via the leakage current. The integrated dose rate was 58 mGy, corresponding to the proton fluence of 8.8×10^7 cm^2. The variations in the dose rate were due to the intended flux changes.

beams provided by PSI-proton irradiation facility (PIF) and TRIUMF-PIF facilities [23], [24], [25]. The presented measurements are further used to demonstrate the capabilities of direct beam characterization, that is, by placing the detector in a beam. The tests in TRIUMF involved 230- and 480-MeV proton beams. In the case of PSI, two primary energies were used: 200 and 70 MeV. Both PSI beams were also further degraded to 151 and 101 MeV (from 200 MeV) and 17 MeV (from 70 MeV). The last one was also further degraded by the Al slabs of 1, 1.2, and 1.5 mm.

A. Energy Deposition Spectra

The setup allows retrieving each single energy deposition event (created by a single hitting particle). Depending on the beam type, the resulting energy deposition spectra provide information concerning the beam energy spread and the interaction of the radiation field with silicon, the latter being essential also for Monte Carlo simulations benchmarking. Examples of energy deposition histograms collected with the aforementioned proton beams are depicted in Fig. 6.

There is a good agreement between the ~200-MeV spectra measured in PSI and TRIUMF. With the decreasing energy, there are fewer open nuclear reaction channels, and therefore fewer high-energy deposition events. In the case of significantly degraded beams, the majority of the measured events are due to proton direct ionization and were not measured by the high-energy proton beam, due to their lower linear energy transfer (LET). Moreover, due to the energy degradation and associated beam energy spread, some protons do and some do not deposit their entire energy in the silicon, leading to the step at ~6 MeV, which corresponds to the maximum energy that can be deposited via dE/dx by protons in the thickness of the diode. The step can be used as an ad hoc calibration in the radiation environment with a significant presence of protons, for example, when the presented calibration is not valid due to additional cable attenuation.

B. Diode as a Flux Monitor

For particle beams with a high probability of interaction with silicon, that is, excluding neutrons, the setup can be used as a flux monitor, as events can be resolved in time. Fig. 7 demonstrates an example of the diode application as a flux monitor, for direct beam characterization. However, the proposed detector has one drawback, namely that some active silicon region is shielded by the metal casing. If no prior assumptions concerning a beam can be made (capability of

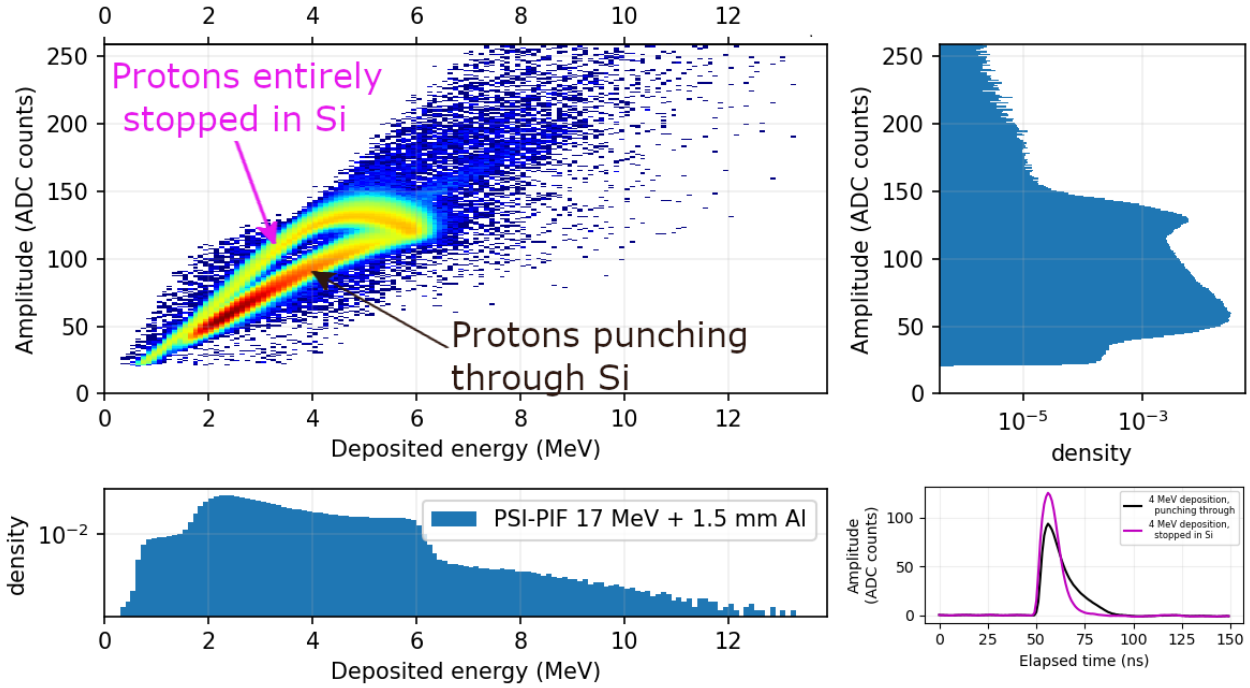

Fig. 9. Amplitude of the energy deposition events as a function of the event deposited energy, as measured with detector I under the 17-MeV proton irradiation, further degraded by 1.5 mm of Al slab. In the bottom right side of the figure, there are averaged pulse shapes, both with 4-MeV deposited energy, one by protons that punched through the case, and the second one that deposited entire energy in silicon.

punching through the casing), the flux measurement is with 70% uncertainty, because of the active surface uncertainty (between 0.75 and 0.85 cm^2). However, in case these events can be identified in energy deposition spectra (e.g., for heavy ions with high LET), the accuracy of the flux measurement is significantly improved.

C. Dose-Rate Estimations

Profiting from the dose rate calibration, described in Section III-B, through the leakage current measurements, the setup can be exploited for a beam characterization, in terms of absolute delivered dose and the time variability. Fig. 8 depicts the dose rate during 230-MeV-proton irradiation at TRIUMF-PIF. Over the irradiation with the total fluence of 8.8×10^7 cm^{-2}, the measured total ionizing dose (TID) was 58.0 mGy. Assuming the LET of the beam is equal to 3.37 MeV cm^2/g [26], the expected dose is 47.4 mGy, within 19% agreement with diode the measurements. According to the FLUKA Monte Carlo simulations for 230-MeV protons, the case could lead up to 3.4% higher dose when compared with uncovered silicon volume. The higher measured value could arise from the calibration, as explained in Section III-B, due to not fully achieved electron equilibrium.

In general, the aforementioned calibration is a good approximation for particles that are capable of penetrating the diode case without significant energy loss. The estimated uncertainty for such mixed fields is within 41%, arising from the difference in the exposed/covered silicon volumes and electron equilibrium during calibration. In the mixed field where there is a significant presence of thermal neutrons, the case would act as a converted and the related deposited dose would be significantly larger as compared with pure silicon.

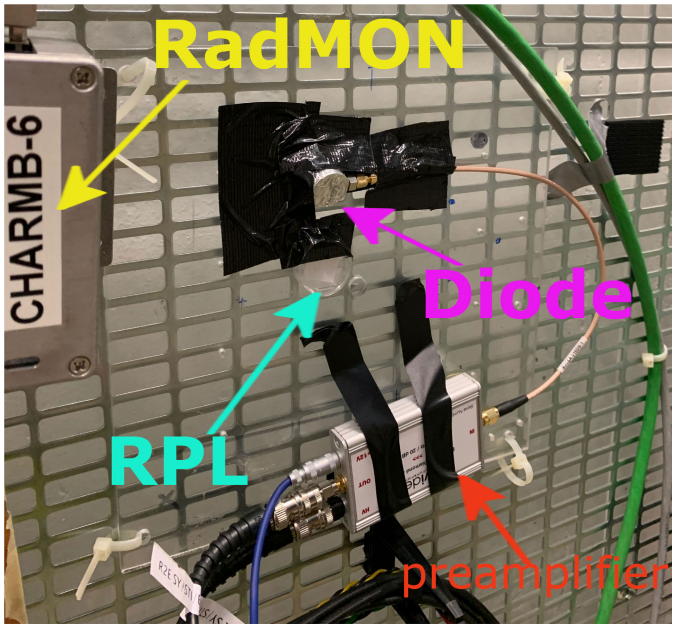

Fig. 10. Silicon diode during experiments in CHARM, in *G*0 position. Additionally, in its direct proximity, RadMON and RPL dosimeters were installed.

D. Event Classification via Pulse Shape Discrimination

The setup allows collecting not only deposited energy values but entire current profiles with 1-ns resolution. This feature can be exploited for pulse shape discrimination (PSD), for example, in terms of amplitude or falling time [27], [28]. Fig. 9 represents the density histogram of amplitudes versus deposited energies for irradiation with 17-MeV proton beam (degraded from 70 MeV), further degraded by 1.5 mm of Al. The corresponding energy deposition spectra are depicted in

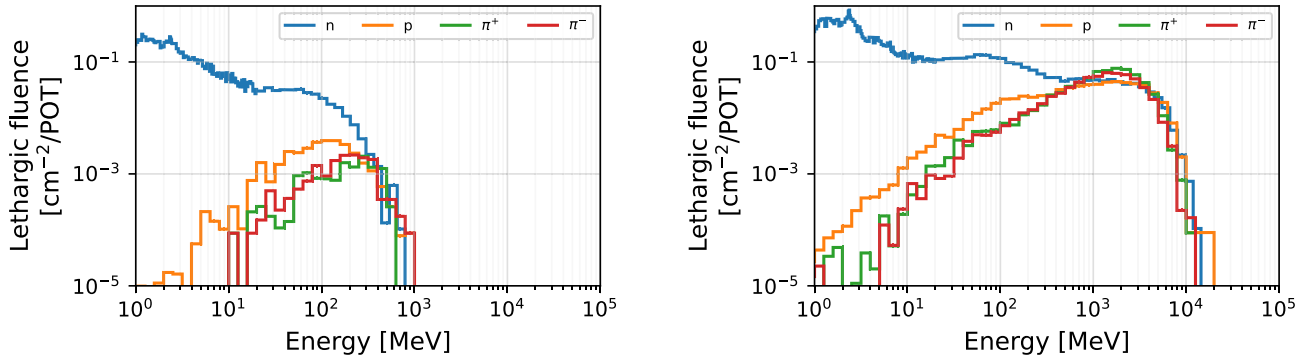

Fig. 11. Simulated particle spectra, for the dominating particle species, in $G0$ (left side) and $m5$ (right side), for CHARM configuration with copper target, and no shielding in place.

Fig. 6. As the beam encountered multiple interactions before reaching the diode, the beam energy spread was expected to be large. For 300-μm silicon thickness, the highest energy that can be deposited through the direct ionization by protons is 6.07 MeV [29], and therefore the particles above this energy mostly punchthrough the silicon volume. A similar conclusion could be drawn based on the analysis of the distribution of the fall time versus deposited energy. The PSD is especially useful during heavy-ion beam characterization for the detection of contaminants [30].

V. CHARM Mixed-Field Measurements

The silicon diode setup during CHARM tests in the $G0$ position is shown in Fig. 10, together with other radiation sensors, covered in Section VI-A. The experimental measurements were collected with detector I during operation with a Cu target and no shielding in place. The related FLUKA Monte Carlo simulations were performed in a two-step approach. In the first one, the entire geometry of the CHARM facility was simulated, and particles were scored in $20 \times 20 \times 20$ cm^3 air volumes located in $G0$ and $m5$ positions. The resulting particle spectra in $G0$ and $m5$ locations, for the most relevant particle species are depicted in Fig. 11. The particle spectrum in $m5$ spans toward higher energies and contains more pions and protons when compared with neutrons. The contribution of EM particles is visible mostly at lower deposited energies, and therefore they were neglected. In the second step, simplified simulations were performed, involving the particle spectra from the first step and the silicon diode model. This approximation neglects the directionality of the radiation in the primary field and particles come as a diode-orthogonal beam. The measurements from $G0$ and $m5$ positions are depicted in Fig. 12, together with FLUKA Monte Carlo simulations. There is a very good agreement at the $G0$ position. In the $m5$ testing position, the agreement between simulation and measurements is worse which could be due to: 1) the use of a two-step simulation approach that neglects the directionality of the radiation field, which is known to introduce discrepancies [31]; 2) other issues with the simulations, for example, related to modeling of the detector's dimensions/materials; 3) radiation degradation or malfunctioning of the silicon detector; and 4) the misplacement with respect to the $m5$ position, as the alignment was performed remotely.

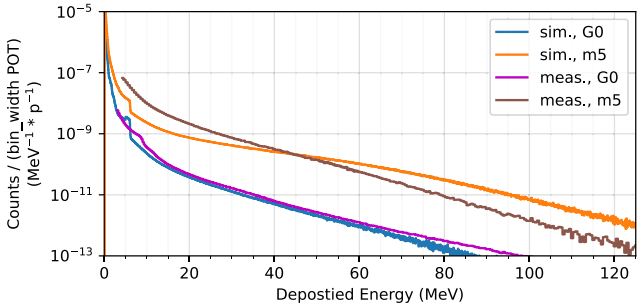

Fig. 12. Measured energy deposition spectra in testing positions $G0$ and $m5$, as measured by detector I at CHARM for the Cu target and no shielding in use. The traces were normalized to the delivered POT. Additionally, simulated energy deposition distribution was depicted, as retrieved via the FLUKA Monte Carlo simulations, considering circular beam composed of particle spectra shown in Fig. 11.

The exact reason remains unknown and the tests should be repeated to confirm that the discrepancy arises from the simulation side.

VI. Indirect Beam Characterization

The detectors can be successfully used for beam characterization. Within this work, we investigate the detector used for indirect beam diagnostics, that is, measuring the secondary field produced through the target, as opposed to the direct exposition of the detector to the primary beam (covered in Section IV). For this purpose, the detectors can be used in two acquisition modes, also simultaneously. The first one measures each energy deposition event. While counting a number of events over time, as illustrated in Section VI-C, the information about the relative beam intensity can be retrieved. Whenever the information about single-energy depositions is not necessary or not available (e.g., due to the digitizer saturation), the second mode can be exploited, as presented in Section VI-A. It makes use of the current that is measured at the output of the preamplifier. With the calibration presented in Section III, the measured current can be converted to the dose rate (Co-60 equivalent).

A. Beam Intensity Through TID Measurements

For constant settings, the TID in each CHARM location will be proportional to the number of protons on the target (POT). In the case of the silicon diode, the leakage current

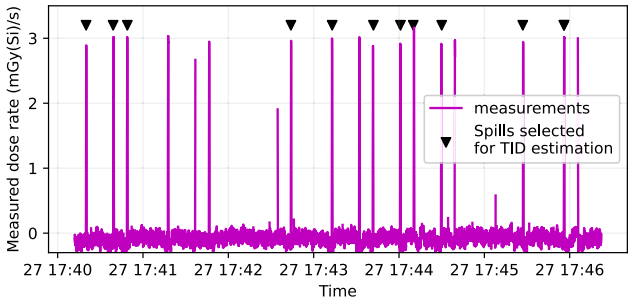

Fig. 13. Dose rate (retrieved through the calibration presented in Section III) over time as measured by detector I in the $G0$ position (CHARM configuration: no shielding in place with the Cu target). Due to a limitation of the source measure unit (no measurement while accessing buffered data), only selected spills were captured entirely and thus used for TID estimation.

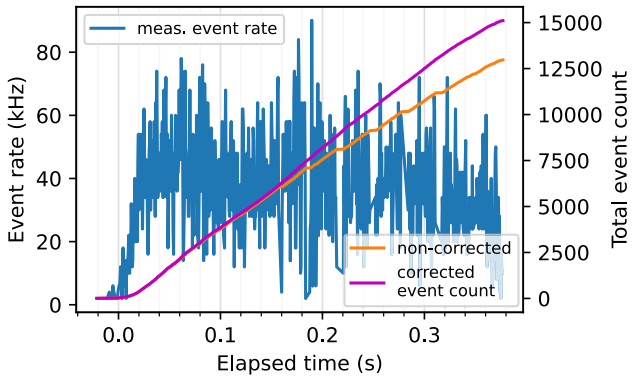

Fig. 14. Example of a spill recorded with the digitizer by means of the event count rate (1 ms binning), together with the raw total event count, and event count that was corrected to compensate for the buffer saturation.

was measured only during several spills, not throughout the entire CHARM run (one week). Within the selected 11 spills, selected among those depicted in Fig. 13, corresponding to 6.49×10^{12} POT, the detector measured 10.96 mGy (1.69×10^{-15} Gy/POT). As the CHARM configuration was constant, extrapolating the following result to the entire one-week run yields (36.04 ± 0.82) Gy (std. error).

Over the corresponding CHARM run (one week), a radiophotoluminescence (RPL) dosimeter [32] was installed very close to the diode, as shown in Fig. 10. During the one week of acquisition, the RPL dosimeter measured 32.6 Gy, that considering the POT $= 2.13 \times 10^{16}$ p, corresponds to a dose rate of 1.53×10^{-15} Gy/POT (copper target and no shielding). At the same time, the nearby RadMON measured 26.9 Gy (1.26×10^{-15} Gy/POT). The agreement of the diode TID measurement is within 25% with RadMON and within 10% once compared with the RPL dosimeter.

Repeating the procedure for all possible shielding/target configurations would allow for indirect beam intensity measurements, through the TID deposited in each spill.

B. Mitigations for High-Intensity Beams

The proposed setup has a limitation concerning the maximum event rate (30 kHz for 500-ns events) due to the bandwidth of the USB 2.0 link between the digitizer and the PC. With the dedicated firmware settings, the number of trigger events can be preserved in the data, providing

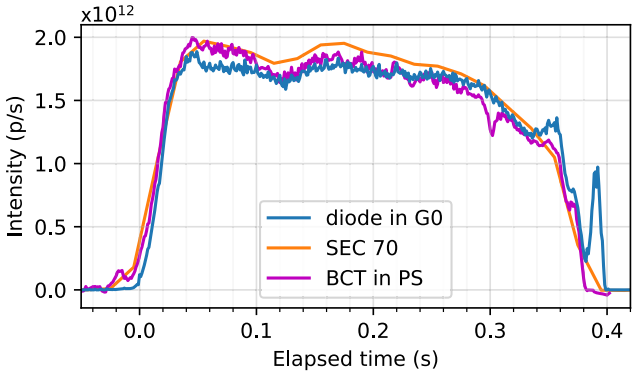

Fig. 15. Averaged spill time profile over 2853 spills as measured via 1) event rate from silicon diode (trigger threshold at 13 ADC counts) in $G0$ position calibrated to secondary emission chamber 70; 2) SEC70; and 3) differentiated signal from the beam current transformer (BCT) in the PS accelerator (before extraction). Whereas the diode measurement was calibrated to the SEC 70 one (total number of counts versus total number of measured protons), the BCT measurement is independent of the other two.

information about how many events were lost due to buffer saturation. This allows retrieving the valid normalization of energy deposition spectra, even in the case of events loss due to the buffer saturation, under the assumption that the composition of the particle spectra is constant in time, enabling the exploitation of the detector as a flux monitor for high-intensity beams, as long as pile-ups are negligible. An example of a spill, collected in CHARM's $G0$ position, when the event rate led to dead time, is depicted in Fig. 14, together with a related dead-time correction.

C. Beam Time Profile From the Event Rate

Assuming the constant test settings (target, shielding, testing position, amplification, and acquisition threshold), the diode detector can be used to resolve the primary beam time profile, through the measured count rate, which is corrected for a dead time, as described in Section VI-B.

As a first step, for the selected test settings, the count rate has to be calibrated against the total beam intensity. Within this study, we used a secondary emission chamber [33] (position 70) that provides an absolute number of protons per spill in the transfer line supplying CHARM with a proton beam. Over the selected time period, 2853 CHARM spills were considered. To cross-calibrate the diode, the total number of counts was divided by the total number of protons delivered to CHARM, leading to the 4.1×10^7 POT/count. This factor was retrieved for a $G0$ position with no shielding and copper target, the analog-to-digital converter (ADC) threshold of 13 ADC counts while running with a CIVIDEC C1-HV amplifier and an additional 6-dB attenuator. The resulting beam time profile is depicted in Fig. 15 and it is in good agreement with the decrease rate of the intensity in the PS accelerator (primarily due to extraction), which is independent of the profile measured by diode through the SEC70 cross-calibration.

The described procedure could be used to assess the beam time profile with a better time resolution than through the SEC70 instrument (20 ms resolution). The direct time profile measurement of the CHARM primary beam, with the diode installed directly in the beam, would lead to quick detector damage.

VII. Conclusion

This article introduced a silicon diode, manufactured by Canberra, with an energy deposition calibration in the few MeV energy ranges and dose rate calibration up to 8 mGy(Si)/s. The detector is commercially available and is widely used in the radiation effects community for heavy-ion beam characterization. Despite the partial coverage of the active silicon (up to 0.35 cm^2) by the detector case, we highlighted several use cases for both beam and radiation characterization, with the related limitations.

As a novelty, based on the CERN CHARM's mixed field, we have demonstrated how the diode can be used indirectly to retrieve key beam characteristics (intensity, time profile) from the secondary radiation field when direct in-beam measurement is not possible.

The benchmark of the experimental measurements in the CHARM *G*0 position yields very good agreement with the FLUKA Monte Carlo simulations. In this position, the measured TID is within 25% when compared to RadMON and within 10% when compared to the RPL dosimeter.

Acknowledgment

The authors would like to thank J. Lendaro, N. Emriskova, and A. Waets for their support with the mechanical integration during CHARM tests in the *m*5 position.

References

[1] R. G. Alía et al., "LHC and HL-LHC: Present and future radiation environment in the high-luminosity collision points and RHA implications," *IEEE Trans. Nucl. Sci.*, vol. 65, no. 1, pp. 448–456, Jan. 2018.

[2] K. Biłko et al., "Radiation environment in the Large Hadron Collider during the 2022 restart and related RHA implications," *IEEE Trans. Nucl. Sci.*, Oct. 2023. [Online]. Available: https://ieeexplore.ieee.org/document/10298830

[3] L. Evans and P. Bryant, "LHC machine," *J. Instrum.*, vol. 3, no. 8, Aug. 2008, Art. no. S08001, doi: 10.1088/1748-0221/3/08/s08001.

[4] K. Bilko et al., "CERN super proton synchrotron radiation environment and related radiation hardness assurance implications," *IEEE Trans. Nucl. Sci.*, vol. 70, no. 8, pp. 1606–1615, Aug. 2023.

[5] J. Mekki, M. Brugger, R. G. Alia, A. Thornton, N. C. D. S. Mota, and S. Danzeca, "CHARM: A mixed field facility at CERN for radiation tests in ground, atmospheric, space and accelerator representative environments," *IEEE Trans. Nucl. Sci.*, vol. 63, no. 4, pp. 2106–2114, Aug. 2016.

[6] D. Di Francesca et al., "Dosimetry mapping of mixed-field radiation environment through combined distributed optical fiber sensing and FLUKA simulation," *IEEE Trans. Nucl. Sci.*, vol. 66, no. 1, pp. 299–305, Jan. 2019.

[7] G. Spiezia, "The LHC radiation monitoring system—RadMon," CERN, Geneva, Switzerland, Tech. Rep. CH-1211, Oct. 2012.

[8] G. Spiezia et al., "A new Radmon version for the LHC and its injection lines," *IEEE Trans. Nucl. Sci.*, vol. 61, no. 6, pp. 3424–3431, Dec. 2014.

[9] A. Ferrari, P. Sala, A. Fasso, and J. Ranft, "FLUKA: A multi-particle transport code," SLAC, Menlo Park, CA, USA, Tech. Rep. SLAC-R-773, Dec. 2005, doi: 10.2172/877507.

[10] T. T. Böhlen et al., "The FLUKA code: Developments and challenges for high energy and medical applications," *Nucl. Data Sheets*, vol. 120, pp. 211–214, Jun. 2014.

[11] C. Ahdida et al., "New capabilities of the FLUKA multi-purpose code," *Frontiers Phys.*, vol. 9, Jan. 2022, Art. no. 788253. [Online]. Available: https://www.frontiersin.org/articles/10.3389/fphy.2021.788253/full

[12] D. Prelipcean et al., "Benchmark between measured and simulated radiation level data at the mixed-field CHARM facility at CERN," *IEEE Trans. Nucl. Sci.*, vol. 69, no. 7, pp. 1557–1564, Jul. 2022.

[13] M. Bagatin et al., "Characterizing high-energy ion beams with PIPS detectors," *IEEE Trans. Nucl. Sci.*, vol. 67, no. 7, pp. 1421–1427, Jul. 2020.

[14] R. G. Alía et al., "Heavy ion energy deposition and SEE intercomparison within the RADNEXT irradiation facility network," *IEEE Trans. Nucl. Sci.*, vol. 70, no. 8, pp. 1596–1605, Aug. 2023.

[15] R. G. Alía et al., "Fragmented high-energy heavy-ion beams for electronics testing," *IEEE Trans. Nucl. Sci.*, vol. 70, no. 4, pp. 486–495, Apr. 2023.

[16] C. Cazzaniga, R. G. Alía, M. Kastriotou, M. Cecchetto, P. Fernandez-Martinez, and C. D. Frost, "Study of the deposited energy spectra in silicon by high-energy neutron and mixed fields," *IEEE Trans. Nucl. Sci.*, vol. 67, no. 1, pp. 175–180, Jan. 2020.

[17] K. Bilko et al., "Silicon solid-state detectors for monitoring high-energy accelerator mixed field radiation environments," in *Proc. 21st Eur. Conf. Radiat. Effects Compon. Syst. (RADECS)*, Sep. 2021, pp. 179–183.

[18] E. Montbarbon et al., "The new CERN east area primary and secondary beams," CERN, Geneva, Switzerland, Tech. Rep. CERN-ACC-2019-234, Jun. 2019, pp. 3730–3733. [Online]. Available: https://accelconf.web.cern.ch/ipac2019/doi/JACoW-IPAC2019-THPGW062.html

[19] Y. Morilla et al., "Progress of CNA to become the Spanish facility for combined irradiation testing in aerospace," in *Proc. 18th Eur. Conf. Radiat. Effects Compon. Syst. (RADECS)*, Sep. 2018, pp. 250–254.

[20] J. Gómez-Camacho et al., "Research facilities and highlights at the Centro Nacional de Aceleradores (CNA)," *Eur. Phys. J. Plus*, vol. 136, no. 3, Mar. 2021, Art. no. 273, doi: 10.1140/epjp/s13360-021-01253-x.

[21] C. Cazzaniga et al., "Measurements of low-energy protons using a silicon detector for application to SEE testing," *IEEE Trans. Nucl. Sci.*, vol. 69, no. 3, pp. 485–490, Mar. 2022.

[22] H. Chabane et al., "Determination of the deposited energy in a silicon volume by *n*-Si nuclear interaction," *J. Appl. Phys.*, vol. 99, no. 12, Jun. 2006, Art. no. 124916, doi: 10.1063/1.2209088.

[23] W. Hajdas, F. Burri, C. Eggel, R. Harboe-Sorensen, and R. de Marino, "Radiation effects testing facilities in PSI during implementation of the Proscan project," in *Proc. IEEE Radiat. Effects Data Workshop*, Jul. 2002, pp. 160–164.

[24] E. W. Blackmore, "Operation of the TRIUMF (20–500 MeV) proton irradiation facility," in *Proc. IEEE Radiat. Effects Data Workshop, IEEE Nucl. Space Radiat. Effects Conf.*, Reno, NV, USA, Jul. 2000, pp. 1–5. [Online]. Available: https://ieeexplore.ieee.org/document/896260/

[25] E. W. Blackmore, P. E. Dodd, and M. R. Shaneyfelt, "Improved capabilities for proton and neutron irradiations at TRIUMF," in *Proc. IEEE Radiat. Effects Data Workshop*, Jul. 2003, pp. 149–155.

[26] NIST. (Oct. 2009). *Stopping-Power & Range Tables for Electrons, Protons, and Helium Ions*. [Online]. Available: https://www.nist.gov/pml/stopping-power-range-tables-electrons-protons-and-helium-ions

[27] G. Pausch et al., "Identification of light charged particles and heavy ions in silicon detectors by means of pulse-shape discrimination," in *Proc. IEEE Nucl. Sci. Symp. Med. Imag. Conf. Rec.*, Oct. 1995, pp. 23–27.

[28] C. Cazzaniga et al., "Measurements of ultra-high energy lead ions using silicon and diamond detectors," *Nucl. Instrum. Methods Phys. Res. A, Accel. Spectrom. Detect. Assoc. Equip.*, vol. 985, Jan. 2021, Art. no. 164671.

[29] J. F. Ziegler, M. D. Ziegler, and J. P. Biersack, "SRIM—The stopping and range of ions in matter (2010)," *Nucl. Instrum. Methods Phys. Res. B, Beam Interact. Mater. At.*, vol. 268, nos. 11–12, pp. 1818–1823, Jun. 2010. [Online]. Available: https://ui.adsabs.harvard.edu/abs/2010NIMPB.268.1818Z

[30] T. Borel et al., "PIPS diode test setup for heavy ion beam spectral characterization," *IEEE Trans. Nucl. Sci.*, vol. 70, no. 8, pp. 1732–1739, Aug. 2023. [Online]. Available: https://ieeexplore.ieee.org/document/10146309/

[31] M. Marzo et al., "RadFET dose response in the CHARM mixed-field: FLUKA MC simulations," *EPJ Nucl. Sci. Technol.*, vol. 3, Jul. 2017, Art. no. 24. [Online]. Available: https://www.epj-n.org/articles/epjn/abs/2017/01/epjn170005/epjn170005.html

[32] D. Pramberger, Y. Q. Aguiar, J. Trummer, and H. Vincke, "Characterization of radio-photo-luminescence (RPL) dosimeters as radiation monitors in the CERN accelerator complex," *IEEE Trans. Nucl. Sci.*, vol. 69, no. 7, pp. 1618–1624, Jul. 2022.

[33] V. Agoritsas, "Secondary emission chambers for monitoring the CERN proton synchrotron ejected beams," in *Proc. Symp. Beam Intensity Meas.*, Daresbury, U.K., Apr. 1968, pp. 117–151. [Online]. Available: https://cds.cern.ch/record/299104/files/CERN-MPS-Int-co-68-9.pdf